RAPID COMMUNICATION

Superconducting properties of the C15-type Laves phase $ZrIr_2$ with an Ir-based kagome lattice

Qing-Song Yang(杨清松)[1,2], Bin-Bin Ruan(阮彬彬)[1,†], Meng-Hu Zhou(周孟虎)[1], Ya-Dong Gu(谷亚东)[1,2], Ming-Wei Ma(马明伟)[1], Gen-Fu Chen(陈根富)[1,2], and Zhi-An Ren(任治安)[1,2,‡]

[1] *Institute of Physics and Beijing National Laboratory for Condensed Matter Physics, Chinese Academy of Sciences, Beijing* 100190, *China*
[2] *School of Physical Sciences, University of Chinese Academy of Sciences, Beijing* 100049, *China*

(Received 28 September 2022; revised manuscript received 2 November 2022; accepted manuscript online 17 November 2022)

We report systematic studies on superconducting properties of the Laves phase superconductor $ZrIr_2$. It crystallizes in a C15-type (cubic $MgCu_2$-type, space group $Fd\bar{3}m$) structure in which the Ir atoms form a kagome lattice, with cell parameters $a = b = c = 7.3596(1)$ Å. Resistivity and magnetic susceptibility measurements indicate that $ZrIr_2$ is a type-II superconductor with a transition temperature of 4.0 K. The estimated lower and upper critical fields are 12.8 mT and 4.78 T, respectively. Heat capacity measurements confirm the bulk superconductivity in $ZrIr_2$. $ZrIr_2$ is found to possibly host strong-coupled s-wave superconductivity with the normalized specific heat change $\Delta C_e/\gamma T_c \sim 1.86$ and the coupling strength $\Delta_0/k_B T_c \sim 1.92$. First-principles calculations suggest that $ZrIr_2$ has three-dimensional Fermi surfaces with simple topologies, and the states at Fermi level mainly originate from the Ir-5d and Zr-4d orbitals. Similar to $SrIr_2$ and $ThIr_2$, spin–orbit coupling has dramatic influences on the band structure in $ZrIr_2$.

Keywords: $ZrIr_2$, superconductivity, Laves phase, kagome lattice, spin–orbit coupling

PACS: 74.25.–q, 74.20.Pq, 74.25.Bt, 71.20.Lp **DOI:** 10.1088/1674-1056/aca3a2

1. Introduction

The well-known Laves phases with general formulas AB_2 constitute a large family in the intermetallic compounds.[1–3] Despite the relatively simple compositions, they hold various crystal structures, intriguing physical properties and hence wide applications, such as magnetic materials,[4,5] hydrogen storage materials,[6,7] and superconducting magnets.[8–10] Thermodynamically stable Laves phases mainly crystallize in three common structures, namely, the hexagonal C14-type (or $MgZn_2$-type), the cubic C15-type (or $MgCu_2$-type), and the hexagonal C36-type (or $MgNi_2$-type). Among them, the C14 and C15 Laves phases were found to be more favorable for the occurrence of superconductivity.[1,11,12] For instance, the C15-type V-based superconductors ($Zr_{1-x}Hf_xV_2$) have been intensively studied as candidates for application in high-field superconducting magnets.[13–15] In addition, several C15-type superconductors such as $CeRu_2$[16,17] and Au_2Pb[18,19] were reported to host possible unconventional superconductivity.

Recently, Ir-based C15-type Laves phases AIr_2 (A = Ca, Sr, Ba, Th) have attracted much interest for the coexistence of superconductivity and strong spin–orbit coupling (SOC) effects.[20–26] Although superconductivity in AIr_2 (A = Ca, Sr, Th) had been discovered before the 1960s,[27] the normal-state and superconducting properties of AIr_2 were not systematically studied until these recent reports. Electronic band structure calculations further revealed that the presence of SOC would strongly affect not only the topology of Fermi surfaces but also the lattice stability.[23] All these results suggest that the C15-type AIr_2 are good platforms to study the interplay between SOC and superconductivity. However, studies on these compounds face challenges since AIr_2 (A = Ca, Sr, Ba, Th) are either unstable in air or contain toxic/radioactive elements.

$ZrIr_2$ is also a C15-type superconductor, whose superconductivity was discovered by Matthias *et al.* in 1961.[11] Subsequent studies focused on the magnetic states of rare-earth dopants in $ZrIr_2$,[28–30] but reports on the superconducting nature of $ZrIr_2$ were scarce. To date, evidence for bulk superconductivity in $ZrIr_2$ has not been revealed, and details of the superconducting properties are still lacking. In particular, thermodynamic measurements on $ZrIr_2$ have never been reported, neither have been the superconducting parameters except for the transition temperature (T_c). Given that $ZrIr_2$ is stable in air, and the element Zr is friendly to both health and environment, it is necessary to examine the bulk superconductivity and to study the superconducting properties in detail.

In this paper, we report the superconducting properties of $ZrIr_2$ based on the measurements of resistivity, magnetic susceptibility, and heat capacity. Bulk superconductivity is confirmed by the heat capacity measurements, and the superconducting parameters are determined for the first time. Moreover, $ZrIr_2$ is possibly an s-wave superconductor with strong electron–phonon coupling. First-principles calculations reveal

†Corresponding author. E-mail: bbruan@mail.ustc.edu.cn
‡Corresponding author. E-mail: renzhian@iphy.ac.cn

© 2023 Chinese Physical Society and IOP Publishing Ltd

the crucial role of SOC and the three-dimensional feature of Fermi surfaces in $ZrIr_2$.

2. Methods

Polycrystalline samples of $ZrIr_2$ were prepared by an arc-melting method. The starting materials were zirconium (powder, 99.5%, may contain trace amount of Hf) and iridium (powder, 99.99%). Zr and Ir were thoroughly mixed in a molar ratio of 1.08:2 before pressed into pellets. A slightly excess amount of Zr was used in order to prevent the formation of $ZrIr_3$. The pellets were then arc-melted in high purity argon atmosphere for at least 8 times with intermediate turnovers. The weight losses after arc-melting were always less than 1%. The ingots obtained were subsequently wrapped with tantalum sheets, sealed into quartz tubes, and annealed at 1430 K for three weeks. The final products showed metallic lusters and were stable in air.

X-ray diffraction (XRD) data were collected on a powdered sample using a PAN-analytical x-ray diffractometer (Cu-$K\alpha$ radiation) at room temperature. Rietveld refinements of the XRD results were carried out using the GSAS package.[31] Measurements of electrical resistivity, as well as heat capacity of the sample were performed on a Quantum Design physical property measurement system (PPMS). While magnetization data were collected on a Quantum Design magnetic property measurement system (MPMS). More details about the measurements can be found elsewhere.[32] Note that all the data in this paper were collected on a sample from the same batch. The magnetization data were corrected by taking the demagnetization factors into account.[33]

First-principles calculations were performed by using the density functional theory (DFT), as implemented in the Quantum ESPRESSO (QE) package.[34] Projector augmented wave pseudopotentials from the PSlibrary were chosen,[35] with exchange–correlation functionals of PBEsol based on the generalized gradient approximation (GGA).[36] The energy cutoffs for the wavefunctions were 70 Ry. A Monkhorst–Pack grid of 16^3 k-points was used in the self-consistent calculation, while a grid of 49^3 k-points was used to calculate the density of states (DOS) and the Fermi surfaces. Before the calculation of charge densities, the cells were fully relaxed till the force on each atom was less than 10^{-4} Ry·Bohr^{-1}. Both the scalar relativistic and the fully relativistic cases were considered in the calculation.

3. Results

3.1. Structural characterization

Figure 1(a) demonstrates the powder XRD pattern of $ZrIr_2$. The pattern can be well refined with a C15-type Laves phase structure ($MgCu_2$-type, space group $Fd\bar{3}m$), indicating the formation of the target phase. The unindexed weak peaks in Fig. 1(a) arise from a small amount (9.8 wt.%) of α-ZrIr impurity. The Rietveld refinement yields cell parameters $a = b = c = 7.3596(1)$ Å, in good agreement with previous reports.[11] Details of the refinement results are summarized in Table 1. The cell parameters from DFT relaxations are also listed. The experimental value of a agrees very well with the theoretical ones. When the SOC effects are taken into account, the discrepancy between experiment (7.3596 Å) and theory (7.3614 Å) is less than 0.03%.

Table 1. Crystallographic parameters of $ZrIr_2$ from Rietveld refinement of XRD.

Chemical formula			$ZrIr_2$		
Formula weight			475.66		
Z			8		
R_p			2.9%		
R_{wp}			4.0%		
Space group			$Fd\bar{3}m$ (No. 227)		
a (DFT relaxed, w/o SOC) (Å)			7.3239		
a (DFT relaxed, with SOC) (Å)			7.3614		
a (experimental) (Å)			7.3596(1)		
V (Å^3)			398.62(2)		
Atom (site)	x	y	z	U_{iso} (0.01 Å^2)	Occupancy
Zr (8b)	0.375	0.375	0.375	0.56(4)	1.0
Ir (16c)	0	0	0	0.79(2)	1.0

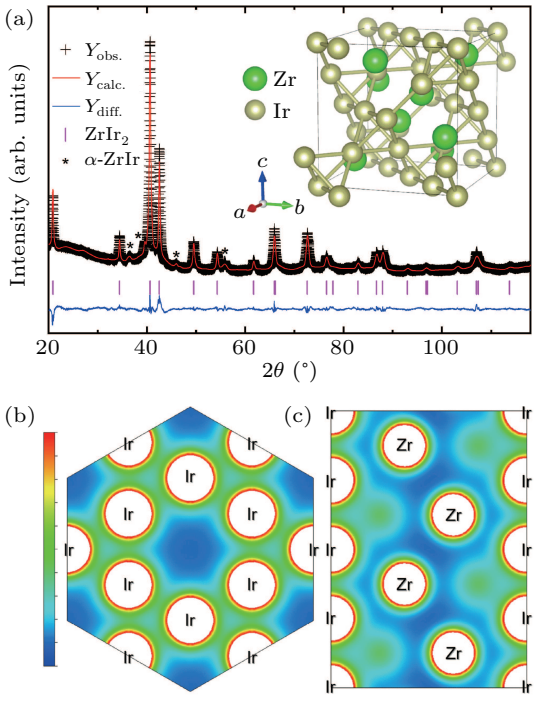


Fig. 1. (a) Room-temperature powder XRD pattern of $ZrIr_2$ and its Rietveld refinements. The conventional unit cell is shown as the inset. (b) Calculated valence charge density (bound between 0 and $0.2e/a_0^3$, where e is the electronic charge and a_0 is the Bohr radius) on the (111) plane. The kagome lattice of Ir atoms is emphasized. (c) Calculated valence charge density on the (110) plane, in which the low-density region around Zr atoms is visible.

The conventional unit cell of $ZrIr_2$ is shown as the inset of Fig. 1(a). The cell is constructed with Zr atoms filling the cavities of the Ir network. Notice the Ir atoms form a kagome

lattice, which is clearly shown in the charge density map in Fig. 1(b). We also note that the Zr–Ir bonds are partially ionic, as the calculated charge density shows "empty" regions surrounding the Zr atoms, as shown in Fig. 1(c). These findings are similar with the cases in isostructural compounds such as $SrIr_2$ or $SrRh_2$.[23]

3.2. Superconducting properties

Figure 2(a) shows the temperature dependence of resistivity (ρ) of $ZrIr_2$ from 1.8 K to 300 K. Metallic behavior can be inferred from the monotonous decrease of ρ to lower temperature, yet the residual resistivity ratio (RRR) is relatively low compared with $SrIr_2$[22,23] or $ThIr_2$.[24] Under zero magnetic field, a sharp superconducting transition is observed below 4.0 K (T_c^{onset}) and ρ becomes zero at 3.8 K (T_c^{zero}). These values are consistent with previous reported T_c (4.1 K) of $ZrIr_2$.[11,27] The transition width is about 0.2 K. In order to estimate the upper critical field ($\mu_0 H_{c2}(T)$), $\rho(T)$ was measured under various magnetic fields, as seen in Fig. 2(b). The superconducting transition is gradually suppressed with the increase of magnetic field. We thus obtain the $\mu_0 H_{c2}(T)$ plot, which is shown in the inset of Fig. 2(a). In the inset, T_c is defined as the midpoint of superconducting transition. $\mu_0 H_{c2}(0)$ is determined to be 4.78 T by a Ginzburg–Landau (G–L) fit: $\mu_0 H_{c2}(T) = \mu_0 H_{c2}(0)[1-(T/T_c)^2]/[1+(T/T_c)^2]$.

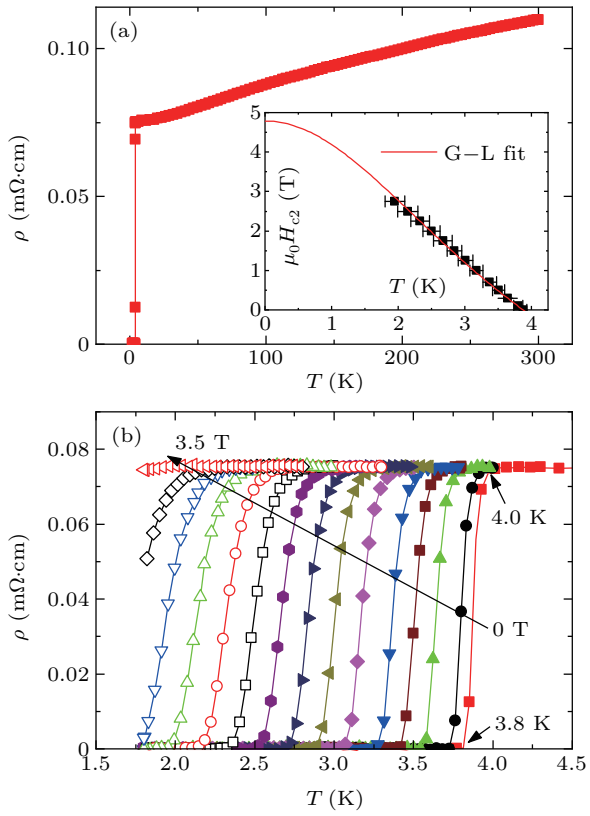


Fig. 2. (a) Temperature dependence of resistivity (ρ) of $ZrIr_2$ in zero magnetic field. Inset shows the temperature dependence of upper critical field ($\mu_0 H_{c2}(T)$). (b) The superconducting transition region on $\rho(T)$ under various magnetic fields up to 3.5 T.

Zero-field-cooled (ZFC) and field-cooled (FC) DC magnetic susceptibility ($4\pi\chi$) of $ZrIr_2$ from 7.0 K to 1.8 K, measured under 10 Oe magnetic field, is demonstrated in Fig. 3(a). The strong diamagnetic signal below 3.8 K indicates the occurrence of superconductivity. The transition temperature is consistent with the one from the $\rho(T)$ measurement. The superconducting shielding fraction from the ZFC curves is ~103%, confirming the bulk nature of superconductivity. The shielding fraction is larger than 100% because of the experimental errors of the sample dimensions. In addition, the existence of strong magnetic flux pinning effects is revealed by the much lower FC signals. The isothermal magnetization curves ($M(H)$) at various temperatures from 1.8 K to 3.6 K are shown in Fig. 3(b). The fields at which the curves deviate 2.5% from the initial Meissner states are defined as the lower critical fields ($\mu_0 H_{c1}$). As a result, the inset of Fig. 3(a) shows the temperature dependence of $\mu_0 H_{c1}$, which can be well fitted with the G–L formula: $\mu_0 H_{c1}(T) = \mu_0 H_{c1}(0)[1-(T/T_c)^2]$, yielding $\mu_0 H_{c1}(0) = 12.8$ mT.

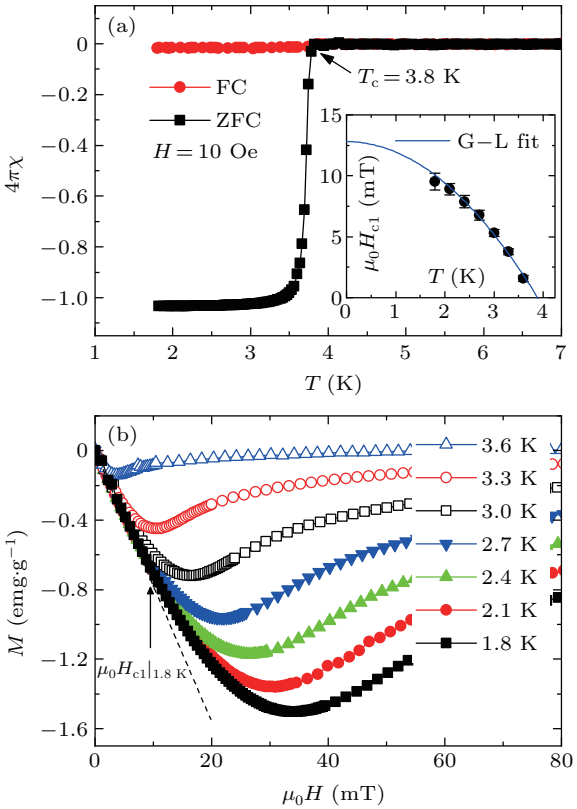


Fig. 3. (a) Temperature-dependent DC magnetic susceptibility of $ZrIr_2$ under 10 Oe. Inset shows the evolution of lower critical field $\mu_0 H_{c1}(T)$. (b) Isothermal magnetization at various temperatures below T_c.

We are able to determine a series of superconducting parameters starting from the values of $H_{c1}(0)$ and $H_{c2}(0)$. The G–L coherence length (ξ_{GL}) is determined to be 8.30 nm by $\mu_0 H_{c2}(0) = \Phi_0/(2\pi\xi_{GL}^2)$, where Φ_0 is the magnetic flux quantum. From the relation[37]

$$\mu_0 H_{c1}(0) = \frac{\Phi_0}{4\pi\xi_{GL}^2}\left[\ln\left(\frac{\lambda_{GL}}{\xi_{GL}}\right) + 0.5\right], \quad (1)$$

the penetration depth (λ_{GL}) and the G–L parameter ($\kappa_{GL} = \lambda_{GL}/\xi_{GL}$) are estimated to be 220.4 nm and 26.6, respectively. κ_{GL} is much larger than $1/\sqrt{2}$, suggesting type-II superconductivity. The thermodynamic field ($\mu_0 H_c(0)$) is thus estimated to be 0.14 T by $H_c^2(0)\ln\kappa_{GL} = H_{c1}(0)H_{c2}(0)$. These superconducting parameters are summarized in Table 2.

We also measured the specific heat of $ZrIr_2$ to examine the superconducting nature. Figure 4(a) shows the temperature dependence of specific heat (C_p) for $ZrIr_2$ within the temperature range of 1.8 K–7.0 K at magnetic fields of zero and 5 T. Notice the C_p data have been corrected by subtracting the contribution of α-ZrIr impurity. The subtraction procedure is similar with that in our previous study.[32] Under zero magnetic field, there was an obvious anomaly on $C_p(T)$ at 3.8 K, validating the bulk nature of superconductivity. The anomaly could be completely suppressed when a field of 5 T was applied. The normal-state $C_p(T)$ measured under 5 T can be well fitted with a Debye model $C_p(T)/T = \gamma + \beta T^2 + \delta T^4$, in which γ is the Sommerfeld coefficient, while the other two terms stand for the phononic contributions. The fitted γ and β values are 8.68 mJ·mol^{-1}·K^{-2} and 0.909 mJ·mol^{-1}·K^{-4}, respectively. And the fitting curve is shown in Fig. 4(a) as the black dash line. Debye temperature (Θ_D) is thus calculated to be 186 K by

$$\Theta_D = \left(\frac{12\pi^4 NR}{5\beta}\right)^{1/3}, \tag{2}$$

in which N is the number of atoms per formula unit (f.u.), and R is the ideal gas constant. The value of Θ_D is comparable with that of $SrIr_2$ (180 K).[22]

We can further estimate the electron–phonon coupling constant λ_{ep} using the McMillan relation[38]

$$\lambda_{ep} = \frac{1.04 + \mu^* \ln(\Theta_D/1.45T_c)}{(1 - 0.62\mu^*)\ln(\Theta_D/1.45T_c) - 1.04}, \tag{3}$$

where μ^* is the Coulomb screening parameter (set to 0.13 in our case). $\lambda_{ep} = 0.68$ is thus obtained, indicating that $ZrIr_2$ hosts a weak to moderate coupling strength. Moreover, the DOS at Fermi level (E_F) is estimated using $N(E_F) = 3\gamma/[\pi^2 k_B^2(1+\lambda_{ep})]$ based on γ and λ_{ep}, yielding $N(E_F) = 2.20$ eV^{-1}·f.u.$^{-1}$.

By subtracting the phononic contributions from C_p, the electronic contribution C_e is obtained and shown in Fig. 4(b). The normalized C_e jump ($\Delta C_e/\gamma T_c$) is determined to be 1.86. This value is larger than the BCS weak-coupling ratio (1.43), suggesting enhanced electron–phonon coupling in $ZrIr_2$. C_e at the superconducting state can be well fitted with the so-called α-model,[39] where $C_e = T\partial S/\partial T$, and the entropy S is expressed as

$$S(T) = -\frac{6\gamma}{\pi^2 k_B}\int_0^\infty [f\ln f + (1-f)\ln(1-f)]\,d\varepsilon, \tag{4}$$

$f = 1/[1+\exp(\sqrt{\varepsilon^2 + \Delta^2(T)}/k_BT)]$, in which $\Delta(T) = \Delta_0 \tanh(1.82[1.018(T_c/T-1)]^{0.51})$. These results mean that $ZrIr_2$ is possibly an s-wave superconductor with an isotropic gap, and the gap value at zero temperature (Δ_0) is fitted to be 0.62 meV. Δ_0/k_BT_c is thus estimated to be 1.92, again validating strong-coupling superconductivity.

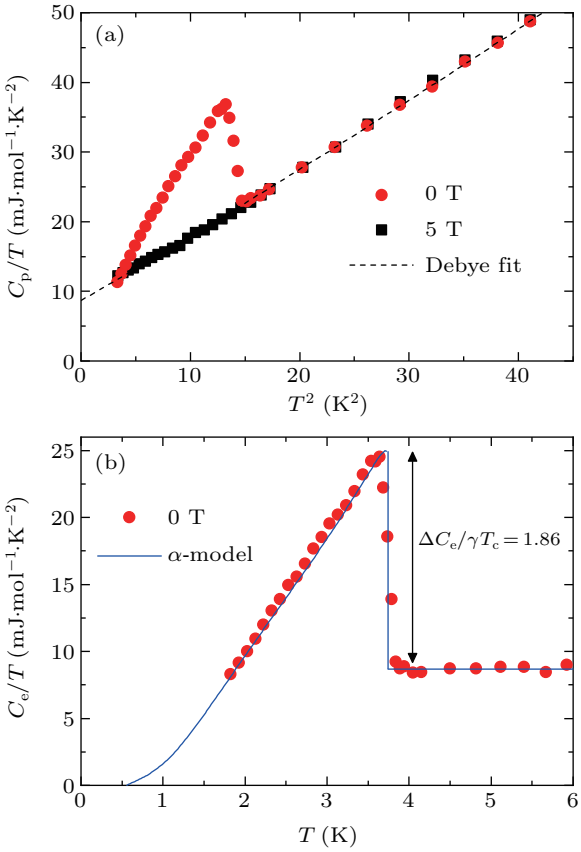


Fig. 4. (a) Specific heat (C_p) for $ZrIr_2$ within the temperature range of 1.8 K–7.0 K under zero and 5 T magnetic field. The black dash line is the fit with Debye model. (b) The electronic contribution of C_p below 6 K. The solid line shows the fit with α-model.

3.3. First-principles calculations

Figure 5(a) shows the electronic band structures of $ZrIr_2$ near E_F from first-principles calculations, in which the results without SOC are plotted as the dash lines, and the SOC results in solid lines. There are three bands crossing E_F both in the absence and presence of SOC, which is consistent with the metallic nature of $ZrIr_2$ from resistivity measurement. Notice the inclusion of SOC dramatically changes the band dispersion near E_F. In particular, band splits are obvious (~ 0.2 eV) at certain k-points, as emphasized by the green circles in Fig. 5(a).

The influences of SOC are also reflected in the DOS plots, as shown in Figs. 5(b) and 5(c). In both cases (with and without SOC), the DOS near E_F are dominated by Ir-5d and Zr-4d orbitals. The strong hybridization between the two orbitals is indicated by the similar shapes of their corresponding contributions. The theoretical value of $N(E_F)$ is 2.94 eV^{-1}·f.u.$^{-1}$

with SOC. This value is slightly larger than the experimental one, which means that the actual E_F is probably lower than calculated. This can be caused by a possible existence of Hf atoms and/or Zr vacancies on the Zr sites.

The three sheets of calculated Fermi surfaces (with SOC) are illustrated in Fig. 5(d). Notice each sheet hosts a Kramers degeneracy. Compared to the isostructural superconductors $SrIr_2$[23] or $ThIr_2$,[24] the Fermi surface topology in $ZrIr_2$ is unexpectedly simple, although they all share three-dimensional features. To be specific, $ZrIr_2$ hosts only one polyhedron-shaped hole-like pocket surrounding the Γ point, plus one capsule-shaped electron-like pocket surrounding the X point.

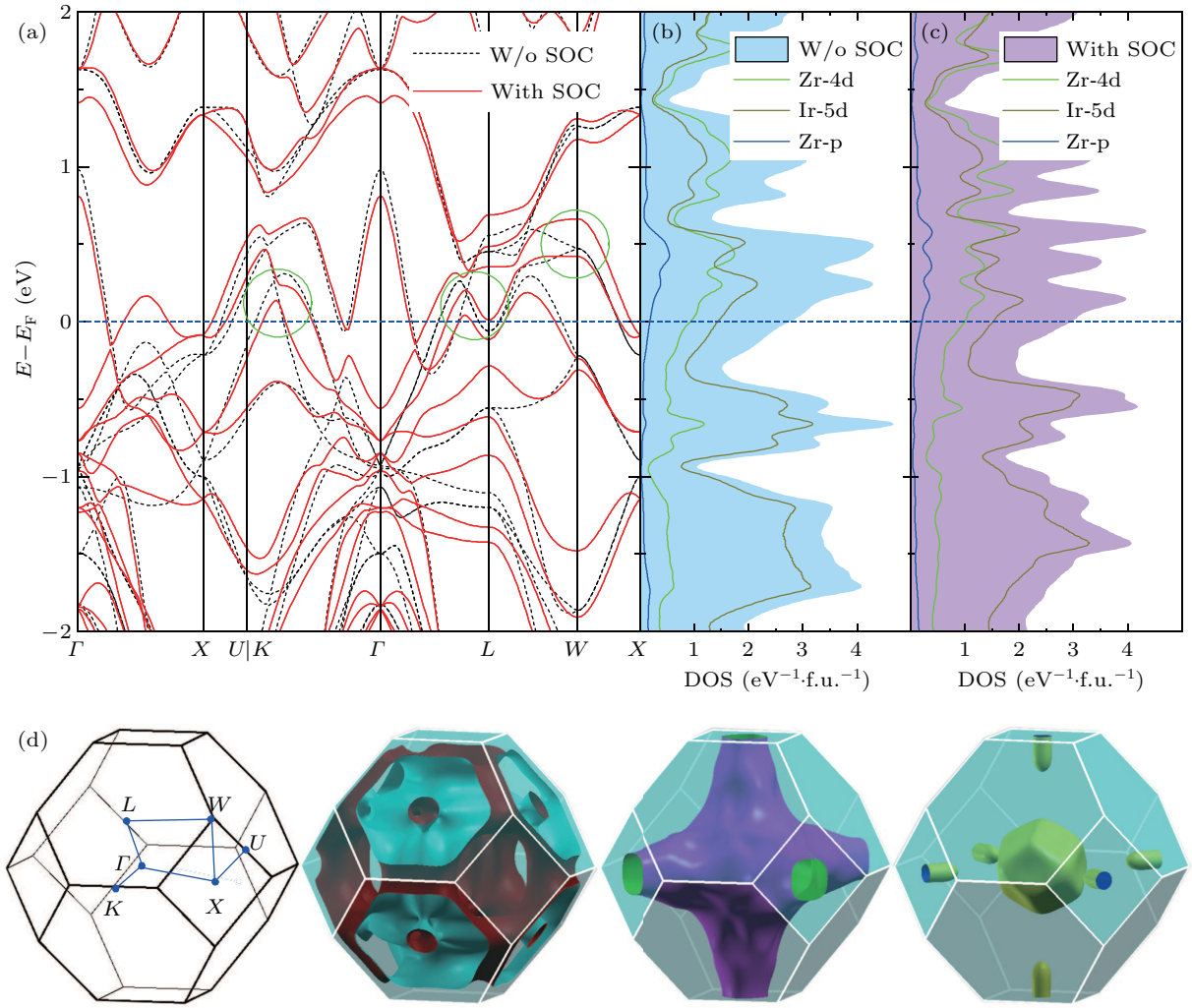


Fig. 5. (a) Calculated electronic band structure of $ZrIr_2$ without and with SOC near the Fermi level. The corresponding DOS plots are shown in (b) and (c), respectively. (d) The high symmetry points in Brillouin zone, and the calculated sheets of Fermi surfaces (with SOC).

4. Discussion

Now we move on to make a comparison between $ZrIr_2$ and C15-type superconductors AIr_2 (A = Ca, Sr, Ba, Th). As shown in Table 2, $N(E_F)$ for $ZrIr_2$ is much lower than the other four members (except for $CaIr_2$). However, T_c of $ZrIr_2$ is comparable with the others'. It is even higher than that of $BaIr_2$ despite the much lower $N(E_F)$ (or γ). Interestingly, we notice that Θ_D is positively correlated with T_c. As Θ_D reflects the phonon dispersion, these results suggest that phonon spectrum, rather than $N(E_F)$, plays an important role in determination of the electron–phonon coupling strength. The modification of phonon spectrum (hence T_c) is realized by changing the guest atom A in the kagome lattice of AIr_2. Indeed, the low-frequency vibrations of the Ir network (kagome lattice), modified by the insertion of Sr, have also been suggested to be the reason for strong electron–phonon coupling in $SrIr_2$.[23] In this respect, future studies on phonon dispersion and electron–phonon interactions in $ZrIr_2$ are needed. Given that the Fermi surfaces of $ZrIr_2$ are quite different (and much simpler) compared with AIr_2 (A = Sr or Th),[23,24] it will possibly provide new thoughts for understanding the superconductivity in Ir-based C15-type superconductors.

Table 2. Superconducting and thermodynamic parameters of $ZrIr_2$. Reference values for AIr_2 (A = Ca, Sr, Ba, Th) are also listed for comparison.

Parameter (unit)	$ZrIr_2$	$CaIr_2$ [20]	$SrIr_2$ [22]	$SrIr_2$ [23]	$BaIr_2$ [25]	$ThIr_2$ [24]
T_c (K)	4.0	5.8	5.9	6.07	2.7	5.58
$\mu_0 H_{c1}(0)$ (mT)	12.8	38.1	10.1	52.2	28.6	9.5
$\mu_0 H_{c2}(0)$ (T)	4.78	4.0	5.9	6.51	6.77	2.25
ξ_{GL} (nm)	8.30	9.07	7.47	7.1	6.97	12.1
λ_{GL} (nm)	220.4	96.0	237	89	152.0	247
κ_{GL}	26.6	10.6	31.7	12.53	21.8	20.4
γ (mJ·mol^{-1}·K^{-2})	8.68	8.36	11.9	15.5	12.0	13.1
β (mJ·mol^{-1}·K^{-4})	0.909	0.32	0.98	0.595	1.83	0.48
Θ_D (K)	186	263	180	214	147	230
λ_{ep}	0.68	0.70	0.84	1.17	0.63	0.72
$\Delta C_e/\gamma T_c$	1.86	0.89	1.71	2.08	1.2	1.19
Experimental $N(E_F)$ (eV^{-1}·f.u.$^{-1}$)	2.20	2.08	2.74	3.03	3.12	3.23

5. Conclusion

In summary, we have systematically investigated superconductivity in the C15-type Laves phase superconductor $ZrIr_2$. Bulk superconductivity with T_c of 4.0 K is confirmed. Our measurements indicate that $ZrIr_2$ is a type-II s-wave superconductor with upper and lower critical fields of 4.78 T and 12.8 mT, respectively. In addition, strong electron–phonon coupling is revealed by the large values of $\Delta C_e/\gamma T_c$ (1.86) and $\Delta_0/k_B T_c$ (1.92). First-principles calculations indicate that the SOC effects are prominent, while the Fermi surface topologies are simple. $ZrIr_2$ is a stable compound under ambient conditions, with health and environmental friendly Zr. Therefore, it serves as a suitable platform, both experimentally and theoretically, to study the interplay between superconductivity and strong SOC in Ir-based C15-type superconductors.

Acknowledgments

Project supported by the National Key Research and Development of China (Grant Nos. 2018YFA0704200 and 2021YFA1401800), the National Natural Science Foundation of China (Grant Nos. 12074414 and 11774402), and the Strategic Priority Research Program of Chinese Academy of Sciences (Grant No. XDB25000000).

References

[1] Compton V and Matthias B T 1959 *Acta Crystallogr.* **12** 651
[2] Hamilton D, Raub C J, Matthias B, Corenzwit E and Hull Jr G 1965 *J. Phys. Chem. Solids* **26** 665
[3] Stein F, Palm M and Sauthoff G 2004 *Intermetallics* **12** 713
[4] Ren W J and Zhang Z D 2013 *Chin. Phys. B* **22** 077507
[5] Samata H, Fujiwara N, Nagata Y, Uchida T and Der Lan M 1999 *J. Magn. Magn. Mater.* **195** 376
[6] Ivey D G and Northwood D O 1986 *Z. Phys. Chem.* **147** 191
[7] Kohlmann H 2020 *Z. Kristallogr. Cryst. Mater.* **235** 319
[8] Inoue K, Kuroda T and Tachikawa K 1979 *IEEE Trans. Magn.* **15** 635
[9] Inoue K, Kuroda T and Tachikawa K 1985 *J. Nucl. Mater.* **133–134** 815
[10] Hishinuma Y, Kikuchi A, Iijima Y, Yoshida Y, Takeuchi T, Nishimura A and Inoue K 2004 *J. Nucl. Mater.* **329–333** 1580
[11] Matthias B, Compton V and Corenzwit E 1961 *J. Phys. Chem. Solids* **19** 130
[12] Stein F and Leineweber A 2021 *J. Mater. Sci.* **56** 5321
[13] Finlayson T and Khan H 1978 *Appl. Phys.* **17** 165
[14] Inoue K, Tachikawa K and Iwasa Y 1971 *Appl. Phys. Lett.* **18** 235
[15] Hishinuma Y, Kikuchi A, Iijima Y, Yoshida Y, Takeuchi T, Nishimura A and Inoue K 2006 *Fusion Eng. Des.* **81** 975
[16] Roy S 1992 *Philos. Mag. B* **65** 1435
[17] Roy S and Chaddah P 1999 *Pramana* **53** 659
[18] Schoop L M, Xie L S, Chen R, Gibson Q D, Lapidus S H, Kimchi I, Hirschberger M, Haldolaarachchige N, Ali M N, Belvin C A, Liang T, Neaton J B, Ong N, Vishwanath A and Cava R 2015 *Phys. Rev. B* **91** 214517
[19] Xing Y, Wang H, Li C K, Zhang X, Liu J, Zhang Y, Luo J, Wang Z, Wang Y, Ling L, Tian M, Jia S, Feng J, Liu X, Wei J and Wang J 2016 *npj Quantum Mater.* **1** 16005
[20] Haldolaarachchige N, Gibson Q, Schoop L M, Luo H and Cava R 2015 *J. Phys.: Condens. Matter* **27** 185701
[21] Yang X, Li H, He T, Taguchi T, Wang Y, Goto H, Eguchi R, Horie R, Horigane K, Kobayashi K, Akimitsu J, Ishii H, Liao Y F, Yamaoka H and Kubozono Y 2019 *J. Phys.: Condens. Matter* **32** 025704
[22] Horie R, Horigane K, Nishiyama S, Akimitsu M, Kobayashi K, Onari S, Kambe T, Kubozono Y and Akimitsu J 2020 *J. Phys.: Condens. Matter* **32** 175703
[23] Gutowska S, Górnicka K, Wójcik P, Klimczuk T and Wiendlocha B 2021 *Phys. Rev. B* **104** 054505
[24] Xiao G, Wu S, Li B, Liu B, Wu J, Cui Y, Zhu Q, Cao G and Ren Z 2021 *Intermetallics* **128** 106993
[25] Koshinuma T, Ninomiya H, Hase I, Fujihisa H, Gotoh Y, Kawashima K, Ishida S, Yoshida Y, Eisaki H, Nishio T and Iyo A 2022 *Intermetallics* **148** 107643
[26] Zhang Y, Tao X M and Tan M Q 2017 *Chin. Phys. B* **26** 047401
[27] Matthias B, Geballe T and Compton V 1963 *Rev. Mod. Phys.* **35** 1
[28] Stein R, Barberis G and Rettori C 1981 *Solid State Commun.* **39** 1157
[29] Slebarski A, Wohlleben D and Weidner P 1985 *Z. Phys. B: Condens. Matter* **61** 177
[30] Slebarski A and Wohlleben D 1985 *Z. Phys. B: Condens. Matter* **60** 449
[31] Toby B 2001 *J. Appl. Crystallogr.* **34** 210
[32] Ruan B B, Sun J N, Chen Y, Yang Q S, Zhao K, Zhou M H, Gu Y D, Ma M W, Chen G F, Shan L and Ren Z A 2022 *Sci. Chin. Mater.* **65** 3125
[33] Prozorov R and Kogan V G 2018 *Phys. Rev. Appl.* **10** 014030
[34] Giannozzi P, Baroni S, Bonini N, Calandra M, Car R, Cavazzoni C, Ceresoli D, Chiarotti G L, Cococcioni M, Dabo I, Dal Corso A, de Gironcoli S, Fabris S, Fratesi G, Gebauer R, Gerstmann U, Gougoussis C, Kokalj A, Lazzeri M, Martin-Samos L, Marzari N, Mauri F, Mazzarello R, Paolini S, Pasquarello A, Paulatto L, Sbraccia C, Scandolo S, Sclauzero G, Seitsonen A P, Smogunov A, Umari P and Wentzcovitch R M 2009 *J. Phys.: Condens. Matter* **21** 395502
[35] Dal Corso A 2014 *Comput. Mater. Sci.* **95** 337
[36] Perdew J P, Ruzsinszky A, Csonka G I, Vydrov O A, Scuseria G E, Constantin L A, Zhou X and Burke K 2008 *Phys. Rev. Lett.* **100** 136406
[37] Hu C R 1972 *Phys. Rev. B* **6** 1756
[38] McMillan W L 1968 *Phys. Rev.* **167** 331
[39] Padamsee H, Neighbor J and Shiffman C 1973 *J. Low Temp. Phys.* **12** 387